Quantifying the effects of EMIC wave scattering and magnetopause shadowing in the outer electron radiation belt by means of data assimilation

S. Cervantes[1,2], Y. Y. Shprits[1,2,3], N. A. Aseev[1,2], and H. J. Allison[1]

[1]Helmholtz Centre Potsdam, GFZ German Research Centre for Geosciences, Potsdam, Germany
[2]Institute of Physics and Astronomy, University of Potsdam, Potsdam, Germany
[3]Department of Earth, Planetary, and Space Sciences, University of California, Los Angeles, CA, USA

Key Points:

- We present a four-year reconstruction of the outer radiation belt based on data assimilation
- In the outer region of the inner magnetosphere, loss due to outward radial diffusion dominates
- At multi-MeV energies, loss due to EMIC waves can dominate in the heart of the outer radiation belt

Corresponding author: S. Cervantes, jscv@gfz-potsdam.de

Abstract

In this study we investigate two distinct loss mechanisms responsible for the rapid dropouts of radiation belt electrons by assimilating data from Van Allen Probes A and B and Geostationary Operational Environmental Satellites (GOES) 13 and 15 into a 3-D diffusion model. In particular, we examine the respective contribution of electromagnetic ion cyclotron (EMIC) wave scattering and magnetopause shadowing for values of the first adiabatic invariant μ ranging from 300 to 3000 MeV G^{-1}. We inspect the innovation vector and perform a statistical analysis to quantitatively assess the effect of both processes as a function of various geomagnetic indices, solar wind parameters, and radial distance from the Earth. Our results are in agreement with previous studies that demonstrated the energy dependence of these two mechanisms. Loss from $L^* = 4$ to $L^* = 4.8$ is dominated by EMIC wave scattering ($\mu \geq 900$ MeV G^{-1}) and may amount to between 10%/hr to 30%/hr of the maximum value of phase space density (PSD) over all L shells for fixed first and second adiabatic invariants. Magnetopause shadowing is shown to deplete electrons across all energies, mostly between $L^* = 5$ and $L^* = 6.6$, resulting in loss from 50%/hr to 70%/hr of the maximum PSD. We also identify a boundary located between $L^* = 3.5$ and $L^* = 5.2$ clearly separating the regions where each mechanism dominates. Nevertheless, during times of enhanced geomagnetic activity, both processes can operate beyond such location and encompass the entire outer radiation belt.

1 Introduction

The physics governing the energetic electrons in the Earth's radiation belts has been subject of considerable research since their discovery in 1959. The outer belt extends from approximately 3 to 7 R_E, is highly dynamic, and can vary by several orders of magnitude on timescales ranging from minutes to weeks. Based on an examination of 276 moderate and intense geomagnetic storms from the period 1989-2000, Reeves et al. (2003) found that storms could either increase, significantly decrease, or not substantially change the fluxes of relativistic electrons in the outer belt. Further studies have associated the variability in the responses of the radiation belts to storms to the complex competing nature between acceleration and loss (e.g., Friedel et al., 2002; Shprits, Elkington, et al., 2008; Shprits, Subbotin, et al., 2008; Millan & Baker, 2012; Turner, Angelopoulos, Li, et al., 2014). Understanding the mechanisms responsible for the acceleration and loss of electrons is indispensable for predicting the response of the radiation belts to geomag-

netic disturbances. In this study we essentially focus on the rapid loss of radiation belt electrons.

It is now widely accepted that reductions of the outer radiation belt electron flux can be attributed both to adiabatic and nonadiabatic processes. Adiabatic processes (H. Kim & Chan, 1997) allow electron fluxes to return to its pre-storm level in the storm recovery phase and radially transport particles in response to a change in the magnetosphere to conserve the three adiabatic invariants (μ, K, Φ). In contrast, many events associated with main-phase dropouts do not recover and fluxes do not return to the original pre-storm values (e.g., McAdams & Reeves, 2001; Reeves et al., 2003). In such cases, the dropout is a result of several different nonadiabatic processes that remove the electrons permanently.

One mechanism that falls into this nonadiabatic category is the loss due to pitch-angle scattering via resonant interaction with various types of magnetospheric waves, including whistler mode chorus, plasmaspheric hiss, and electromagnetic ion cyclotron (EMIC) waves, which leads to electron precipitation to the atmosphere (e.g., Thorne & Kennel, 1971; Lyons et al., 1972; Thorne et al., 2005; Millan et al., 2007; Thorne, 2010; Turner, Angelopoulos, Li, et al., 2014). Another nonadiabatic process is the loss across the magnetopause, called magnetopause shadowing. This term describes the scenario in which the magnetopause moves inward due to increases in solar wind dynamic pressure, resulting in the depletion of electrons on open drift paths that were previously closed (e.g., K. Kim et al., 2008; Ohtani et al., 2009; Morley et al., 2010; Turner et al., 2012). In addition, the loss to the magnetopause generates a sharp gradient that further drives electron outwards and through the magnetosphere, a process known as outward radial diffusion (Shprits et al., 2006). Nevertheless, the relative contribution of each physical process to electron flux dropouts still remains a fundamental puzzle.

Multisatellite observations provide a useful means of understanding the dominant loss mechanisms of radiation belt dropouts. For instance, Green et al. (2004) used 52 dropout events and tested several processes that may contribute to electron flux decreases, including adiabatic motion, magnetopause shadowing, and precipitation to the atmosphere. Their study concluded that the most likely cause of the dropout was precipitation to the atmosphere, although the cause of the precipitation remained uncertain. Turner et al. (2012) analyzed data collected by several spacecraft and concluded that the sudden elec-

tron depletion on 6 January 2011 was mainly a result of outward radial diffusion rather than loss to the atmosphere. Bortnik et al. (2006) studied the relativistic electron dropout on 20 November 2003 and suggested that it was caused by two separate mechanisms that operate at high and low L shells. At $L > 5$ loss was dominated by magnetopause shadowing and outward radial diffusion, whereas at $L < 5$ it was dominated by pitch angle scattering driven by EMIC waves. Similarly, Turner, Angelopoulos, Li, et al. (2014) and Turner, Angelopoulos, Morley, et al. (2014) studied the 30 September 2012 dropout event and concluded that both loss mechanisms operated, with a boundary at $L^* \sim 4$. More recently, Xiang et al. (2017) investigated three distinct radiation belt dropouts observed by Van Allen Probes, subtracting the electron phase space density (PSD) versus L^* profiles before and after the dropout. Their findings suggest that these events can be classified in three different classes in terms of dominant loss processes: magnetopause shadowing dominant, EMIC wave scattering dominant, and a combination of both mechanisms. However, one limitation of in-situ data is the sparse coverage, as incomplete profiles may hinder the calculation of PSD drops.

On the other hand, radiation belt modeling studies have also focused on the importance of loss processes in flux dropouts. For example, Shprits et al. (2006) explored the viability of outward radial diffusion loss by comparing radial diffusion model simulations with CRRES measurements. The comparison showed that nonadiabatic flux dropouts near geosynchronous orbit can be effectively propagated by the outward radial diffusion down to $L^* = 4$ and that magnetopause loss coupled with the radial transport can account for the main-phase flux dropout. Su et al. (2011) examined the contribution of different loss processes by comparing CRRES observations with a three dimensional (3-D) radiation belt model by gradually incorporating magnetopause shadowing, adiabatic transport, radial diffusion, and plume and chorus wave-particle interactions into the code. Yu et al. (2013) quantified the relative contribution of magnetopause shadowing coupled with outward radial diffusion by comparing radial diffusion simulations with GPS-observed total flux dropout. Their results indicated that such process accounted for 60-90%/hr of the main-phase radiation belt electron dropout near geosynchronous orbit.

In the current study, we quantify the contribution of (1) pitch-angle scattering driven by EMIC waves and (2) magnetopause shadowing. We aim to answer the question: how much loss is caused by each mechanism? We tackle this issue with a novel approach based on the assimilation of spacecraft data in a 3-D diffusion model by means of a split-operator

Kalman filter (KF) (Shprits, Kellerman, et al., 2013). In this way, data assimilation (DA) combines spacecraft data and our model predictions in a two-way communication, such that our model corrects inaccurate measurements and fills the gaps where electron PSD measurements are lacking (a constraint in observational studies), and observations bring our model closer to reality. We perform multiple four-year long-term runs (for the period 1 October 2012 to 1 October 2016 spanning different levels of geomagnetic activity) by switching on and off in the model the above-mentioned mechanisms. We quantify their effect by means of the innovation vector, a measure on how observations and model predictions differ, for various values of the adiabatic invariants μ and K.

The outline of this paper is as follows. A brief description of data assimilation and the methodology followed in this study are presented in section 2. We show the long-term reanalysis results of electron PSD in section 3 and the statistical analysis of the effect of scattering by EMIC waves and magnetopause shadowing employing the innovation vector in section 4. Results are discussed in Section 5 and conclusions are presented in section 6.

2 Methodology and data

2.1 VERB code

The current study builds upon the previous work of Shprits, Kellerman, et al. (2013), Kellerman et al. (2014) and Cervantes et al. (2020) and adopts the 3-D Versatile Electron Radiation Belt Code (VERB-3D; Shprits et al., 2009; Subbotin & Shprits, 2009) to assimilate spacecraft data at different locations. The VERB-3D code models the evolution of electron PSD by solving the modified 3-D Fokker-Planck diffusion equation that incorporates radial diffusion, energy diffusion, pitch angle scattering, and mixed diffusion into the drift- and bounce-averaged particle PSD (Schulz & Lanzerotti, 1974). The 3-D Fokker-Planck equation for the evolution of PSD can be written in terms of the L shell, equatorial pitch angle α_0, and relativistic momentum p, following Shprits et al. (2009) and Subbotin and Shprits (2009):

$$\begin{aligned}\frac{\partial f}{\partial t} &= L^{*^2}\frac{\partial}{\partial L^*}\bigg|_{\mu,J}\left(\frac{1}{L^{*^2}}D_{L^*L^*}\frac{\partial f}{\partial L^*}\bigg|_{\mu,J}\right)+\frac{1}{p^2}\frac{\partial f}{\partial p}\bigg|_{\alpha_0,L^*}p^2\left(D_{pp}\frac{\partial f}{\partial p}\bigg|_{\alpha_0,L^*}+D_{\alpha_0 p}\frac{\partial f}{\partial \alpha_0}\bigg|_{p,L^*}\right)\\ &+\frac{1}{T(\alpha_0)\sin(2\alpha_0)}\frac{\partial}{\partial \alpha_0}\bigg|_{p,L^*}T(\alpha_0)\sin(2\alpha_0)\left(D_{\alpha_0\alpha_0}\frac{\partial f}{\partial \alpha_0}\bigg|_{p,L^*}+D_{\alpha_0 p}\frac{\partial f}{\partial p}\bigg|_{\alpha_0,L^*}\right)-\frac{f}{\tau} \quad (1)\end{aligned}$$

where f is electron PSD, μ and J are the first and second adiabatic invariants, respectively, and L^* is inversely related to the third adiabatic invariant Φ. $D_{L^*L^*}$, D_{pp}, $D_{\alpha_0\alpha_0}$, and $D_{\alpha_0 p}$ are the bounce-averaged radial, momentum, pitch angle, and mixed pitch angle-momentum diffusion coefficients, respectively. $T(\alpha_0)$ is a function related to the particle's bounce time (Lenchek et al., 1961; Schulz & Lanzerotti, 1974):

$$T(\alpha_0) = 1.3802 - 0.3198(\sin\alpha_0 + \sin^{1/2}\alpha_0) \tag{2}$$

The parameter τ is a loss rate assumed to be infinite outside the loss cone and equal to a quarter of the electron bounce time inside the loss cone. Readers are referred to Shprits et al. (2009) and Subbotin and Shprits (2009) for a more detailed description of the VERB-3D model.

Based on the previous findings of Drozdov, Shprits, Aseev, et al. (2017) and Wang et al. (2019), who meticulously studied the sensitivity of various parameterizations of radial diffusion, we employ the magnetic radial diffusion rates $D_{L^*L^*}$ of Brautigam and Albert (2000). The parameters for dayside and nightside chorus are taken from Orlova and Shprits (2014), while for hiss the parameterization of Orlova et al. (2014) is used. The location of the plasmapause is calculated following Carpenter and Anderson (1992). The spectral properties from Meredith et al. (2014) are used to calculate diffusion coefficients for helium band EMIC waves, and they are included in the simulation when the solar wind dynamic pressure is greater than or equal to 3 nPa (Drozdov, Shprits, Usanova, et al., 2017). The VERB-3D code includes the Last Closed Drift Shell (LCDS) as a function of time and invariant K. As in Cervantes et al. (2020), physics associated with magnetopause shadowing are introduced using the LCDS. In this study, we use an energy-dependent loss mechanism, since the rate of loss following a reduction in the LCDS depends on the particle's drift period. We employ the Tsyganenko and Sitnov (2007) magnetic field model incorporated into the IRBEM library (Boscher et al., 2012) to determine the LCDS, and we simulate loss due to magnetopause shadowing with an exponential decay of the electron PSD outside the LCDS, as:

$$f(t, L^* > \mathrm{LCDS}(t)) = f(t)e^{(-1/\tau_d)} \tag{3}$$

where, τ_d is the electron drift period calculated as Walt (2005):

$$\tau_{\mathrm{d}}(s) = C_{\mathrm{d}} \left(\frac{\mathrm{R_E}}{R_0}\right) \frac{1}{\gamma\beta^2} \left[1 - 0.333\,(\mathrm{sin}\alpha_0)^{0.62}\right] \tag{4}$$

Here, $\beta = \frac{v}{c}$, $\gamma = (1-\beta^2)^{-1/2}$, $C_{\mathrm{d}} = 1.557{\times}10^4$ for electrons, $\mathrm{R_E} = 6.37{\times}10^3$ km, and R_0 is the distance from the center of the Earth to the equatorial crossing point of a magnetic field line. As the electron energy increases, the drift period decreases.

The size of the computational grid is 29 × 101 × 91 points along radial, energy, and pitch angle dimension, respectively. Radial grid points are distributed uniformly, whereas energy and pitch angle grid points are distributed logarithmically. The L^* grid is set from 1 R_E to 6.6 R_E. The energy grid is defined by a minimum of 0.01 MeV and a maximum of 10 MeV at the outer radial boundary. The pitch angle grid extends from 0.3°to 89.7°.

For the solution of equation (1), the initial PSD is taken from the steady state solution of the radial diffusion equation. A lower radial boundary condition ($L^* = 1$) of $f = 0$ is used in order to simulate the loss of electrons to the atmosphere. The PSD required for the upper radial boundary condition ($L^* = 6.6$) is obtained from Geostationary Operational Environmental Satellites (GOES) observations. The upper energy boundary at 10 MeV is set equal to zero. For the lower energy boundary, the PSD is set constant in time to represent a balance of convective sources and loss. The lower pitch angle boundary condition is set to zero to simulate precipitation loss of electrons into the loss cone in a weak diffusion regime. A zero gradient is chosen to account for the flat pitch angle distribution observed at 90° (Horne et al., 2003) for the upper pitch angle boundary condition.

2.2 Instrumentation and data

We use simultaneous measurements of four spacecraft, the twin Van Allen Probes (renamed from Radiation Belt Storm Probes after launch) A and B, and GOES 13 and 15, covering a four-year period from 1 October 2012 to 1 October 2016. For data assimilation, observations are converted from flux to PSD in phase space coordinates (L^*, μ, K). In-situ magnetic field measurements are employed to calculate μ, while the Tsyganenko and Sitnov (2007) model is employed to calculate K and L^*.

On board the Van Allen Probes (Mauk et al., 2012; Stratton et al., 2012), the Radiation Belt Storm Probes-Energetic particle, Composition, and Thermal plasma (RBSP-ECT) suite measures particles with energies ranging from hot to ultrarelativistic (Spence

et al., 2013). In this study, we utilize measurements from the Magnetic Electron Ion Spectrometer (MagEIS) (Blake et al., 2013), which provides data in the energy range ~ 30 keV to about 4 MeV and Relativistic Electron Proton Telescope (REPT) (Baker et al., 2012) instruments, which covers energies from 2 MeV to tens of MeV. The pitch angle distribution is interpolated in a uniform grid with a step of 5°.

In addition, from satellites 13 and 15 of the multi-mission GOES spacecraft (Onsager et al., 1996; Singer et al., 1996) we employ data from the MAGnetospheric Electron Detector (MAGED; Hanser, 2011) and Energetic Proton, Electron, and Alpha Detector (EPEAD; Onsager et al., 1996; Hanser, 2011) instruments. Nine solid-state-detector telescopes from MAGED provide pitch-angle resolved in-situ electron flux measurements in five energy bands: 30 - 50, 50 - 100, 100 - 200, 200 - 350, and 350 - 600 keV. Four telescopes are oriented in the north-south plane, and the other five in the east-west plane (Hanser, 2011; Rodriguez, 2014a). Moreover, two EPEAD detectors (Onsager et al., 1996; Hanser, 2011) on board each spacecraft measure MeV electron and solar proton fluxes in two energy ranges: > 0.8 MeV and > 2 MeV. One detector is oriented westward and the other eastward (Rodriguez, 2014b). MAGED and EPEAD observations at a five-minute cadence are averaged over one hour. EPEAD integral fluxes are obtained by averaging the measurements over the westward and eastward telescopes, so that the resulting pitch angles are averages between both directions of the two telescopes as well. Integral fluxes as a function of energy are fitted to a power law which is used to interpolate between values up to 1 MeV. In order to convert to differential flux, we employ the 90°pitch angle differential flux data from MAGED and fit the two integral channels of EPEAD to an exponential function $f = A{*}\exp(B{*}E)$, where f is the differential flux, E is the energy, and A and B are positive time-dependent coefficients obtained by solving the flux integral for averaged MAGED data. The pitch angle distribution below 500 keV is directly measured by MAGED.

2.3 Data assimilation and innovation vector

Data assimilation is an algorithm which aims to smoothly blend sparse and inaccurate measurements with dynamical information from a physics-based model. Several DA methods have been developed, such as the Kalman filter in its standard (Kalman, 1960), extended (Jazwinski, 1970), and ensemble versions (Evensen, 1994). The KF is a powerful sequential data assimilation method that combines a numerical model and

incomplete measurements, while minimizing mean-squared errors (Kalman, 1960). The methodology of the standard KF is briefly outlined below.

A system of evolution equations may be presented in the following form:

$$\mathbf{x}_k^f = \mathbf{M}_{k-1}\mathbf{x}_{k-1}^a \tag{5}$$

where $\mathbf{x}$ represents a model state vector (for our model, it is the PSD on the numerical grid locations), and the model matrix $\mathbf{M}$ advances the state vector $\mathbf{x}$ in discrete time increments. The subscript k shows the time step, and superscripts f and a refer to forecast and analysis, respectively. The evolution of $\mathbf{x}_k^t$ (superscript t refers to true), is assumed to differ from the model by a random error ϵ^m:

$$\mathbf{x}_k^t = \mathbf{M}_{k-1}\mathbf{x}_{k-1}^t + \epsilon_k^m \tag{6}$$

where ϵ_k^m is assumed to be a Gaussian white-noise sequence, with mean zero and model-error covariance matrix $\mathbf{Q}$.

The observations $\mathbf{y}_k^o$ (superscript o refers to observed), are assumed to be contaminated by observational errors ϵ_k^o:

$$\mathbf{y}_k^o = \mathbf{H}_k\mathbf{x}_k^t + \epsilon_k^o \tag{7}$$

where ϵ_k^o is also assumed to be Gaussian, white in time, with mean zero and given covariance matrix $\mathbf{R}$. The observation matrix $\mathbf{H}_k$ accounts for the fact that usually the dimension of $\mathbf{y}_k^o$ is less than the dimension of $\mathbf{x}_k^t$.

During the so-called update times, when observations are available, forecast and observations are blended to yield the analysis state vector:

$$\mathbf{x}_k^a = \mathbf{x}_k^f + \mathbf{K}_k(\mathbf{y}_k^o - \mathbf{H}_k\mathbf{x}_k^f) \tag{8}$$

where the term $\mathbf{K}_k\left(\mathbf{y}_k^o - \mathbf{H}_k\mathbf{x}_k^f\right)$ is usually referred to as the innovation vector $\mathbf{x}_k^i$. $\mathbf{K}_k$ is the Kalman gain matrix computed at each time step using a time-evolving forecast error covariance matrix $\mathbf{P}_k^f$ given by:

$$\mathbf{P}_k^f = \mathbf{M}_{k-1}\mathbf{P}_{k-1}^a\mathbf{M}_{k-1}^T + \mathbf{Q}_{k-1} \tag{9}$$

The Kalman gain matrix $\mathbf{K}_k$ represents the optimal weights given to the observations when updating the model state vector:

$$\mathbf{K}_k = \mathbf{P}_k^f\mathbf{H}_k^T\left(\mathbf{H}_k\mathbf{P}_k^f\mathbf{H}_k^T + \mathbf{R}_k\right)^{-1} \tag{10}$$

The error covariance matrix is also updated as follows:

$$\mathbf{P}_k^a = \left(\mathbf{I} - \mathbf{K}_k\mathbf{H}_k\right)\mathbf{P}_k^f \tag{11}$$

The innovation vector $\mathbf{x}_k^i$ warrants a more detailed discussion as this is the term where, in our case, source and loss processes are effectively incorporated into the KF. The innovation vector measures how much new and additional information, provided by the data (hence its name), will modify the model forecast $\mathbf{x}^f$ in order to produce an optimal estimate of the state of the system $\mathbf{x}^a$. The value and the sign of the innovation vector depend on how much the modeled and observed values differ from each other, and on the estimated forecast and observational errors. A perfect model would predict exactly the incoming observations, and the innovation would be zero. As the forecast error covariance matrix $\mathbf{P}_k^f$ approaches zero, the innovation is weighted less heavily by the gain $\mathbf{K}_k$. In contrast, as the observational error covariance matrix $\mathbf{R}_k$ tends to zero, the Kalman gain $\mathbf{K}_k$ weights the innovation more heavily. Shprits et al. (2007), Koller et al. (2007), Daae et al. (2011), and Cervantes et al. (2020) demonstrated the usefulness of the innovation vector to identify and adjust for unknown, missing physics in radiation belt models in order to reduce the discrepancy between observations and model predictions. All of the above-mentioned studies employed the innovation vector to infer acceleration and loss processes for short-term intervals or specific events.

In this paper, we perform a four-year statistical analysis of the innovation vector and employ it as a tool to quantify the loss effect of EMIC wave scattering and magnetopause shadowing on radiation belt electrons. For that purpose, we perform three data assimilation runs (Table 1). The first run includes all processes in our model (hereinafter, "full" run), and in the second and third runs, one process is neglected in each. The "full"

Table 1. Summary of data assimilation runs

Run	Processes included
1	Radial diffusion due to ULF waves + pitch angle, energy, and mixed pitch angle-energy diffusion due to chorus and hiss waves + EMIC wave scattering + magnetopause shadowing, i.e. "full" run
2	Radial diffusion due to ULF waves + pitch angle, energy, and mixed pitch angle-energy diffusion due to chorus and hiss waves + magnetopause shadowing
3	Radial diffusion due to ULF waves + pitch angle, energy, and mixed pitch angle-energy diffusion due to chorus and hiss waves + EMIC wave scattering

simulation (number 1) accounts for: radial diffusion due to ULF waves, pitch angle, energy, and mixed pitch angle-energy diffusion due to chorus and hiss waves, EMIC wave scattering, and magnetopause shadowing. The second run (number 2) accounts for all processes except for scattering by EMIC waves. Finally, the third run (number 3) includes all processes in the "full run" with the exception of magnetopause shadowing. The time step of our VERB simulations is one hour, and assimilation of spacecraft data is performed at the same cadence.

For each of the three runs, we calculate the hourly innovation vector $\mathbf{x}_k^i$ at each L^* and normalize it by the corresponding hourly maximum value of assimilated PSD $\mathbf{x}_k^a$ (from the "full" run) over all L^*. Afterwards, the difference between the absolute values of the normalized innovation of the "full" simulation and the one excluding either loss process is calculated according to the following equation:

$$\Delta\mathbf{x}_k^i = \frac{|\mathbf{x}_{1,k}^i| - |\mathbf{x}_{2,k}^i|}{\max(\mathbf{x}_{1,k}^a)} \times 100\% \tag{12}$$

where subscript 1 refers to the "full" run and subscript 2 to the run lacking either EMIC wave scattering or magnetopause shadowing. Negative values of $\Delta\mathbf{x}_k^i$ indicate that the inclusion of such mechanisms provides a better agreement with the observed PSD, bringing the model prediction closer to reality. On the other hand, positive $\Delta\mathbf{x}_k^i$ suggests that the modeled effect of either process is stronger than observed, hence the ensuing loss is overestimated. In section 4 we interpret the quantity $\Delta\mathbf{x}_k^i$ as an indicator of the loss brought

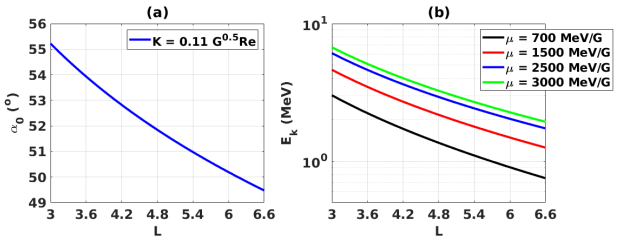

Figure 1. Dependence of equatorial pitch angle α_0 (a) and electron kinetic energy E_k (b) on L shell in a dipolar magnetic field, for the four pairs of (μ, K) investigated in the present study.

by both scattering by EMIC waves and magnetopause shadowing into the dynamics of the outer radiation belt.

3 Long-term reanalysis of electron PSD

In this section we present the results obtained for the radial profiles of PSD based on the assimilation of the above-mentioned four-satellite measurements into the VERB-3D model for the four-year period starting on 1 October 2012. We mainly focus on four pairs of (μ, K) and show the corresponding equatorial pitch angle α_0 and electron kinetic energy E_k in a dipolar magnetic field, in Figure 1. At the heart of the outer radiation belt ($L = 4.5$), for the chosen values of $K = 0.11$ G$^{0.5}$ R$_\mathrm{E}$, the equatorial pitch angle is approximately 52°. Electron energies at $L = 4.5$ are 1.53 MeV for $\mu = 700$ MeV G^{-1}, 2.42 MeV for $\mu = 1500$ MeV G^{-1}, 3.25 MeV for $\mu = 2500$ MeV G^{-1}, and 3.6 MeV for $\mu = 3000$ MeV G^{-1}.

Panels (a) and (c) of Figure 2 show measured Van Allen Probes and GOES hourly averaged electron PSD at $\mu = 700$ MeV G^{-1} and $K = 0.11$ G$^{0.5}$ R$_\mathrm{E}$ and $\mu = 3000$ MeV G^{-1} and $K = 0.11$ G$^{0.5}$ R$_\mathrm{E}$, respectively. The results of the "full" data assimilation run are illustrated in panels (b) and (d). The assimilated PSD is consistent with the original spacecraft data and it indicates the improvement in coverage that reanalysis provides. Panels (e) and (f) depict the solar wind dynamic pressure P_{dyn} and the geomagnetic indices Kp and Dst. The data assimilation runs for electron PSD at $\mu = 1500$ MeV G^{-1} and $K = 0.11$ G$^{0.5}$ R$_\mathrm{E}$ and $\mu = 2500$ MeV G^{-1} and $K = 0.11$ G$^{0.5}$ R$_\mathrm{E}$ are shown in Figure A1 in the supplementary material.

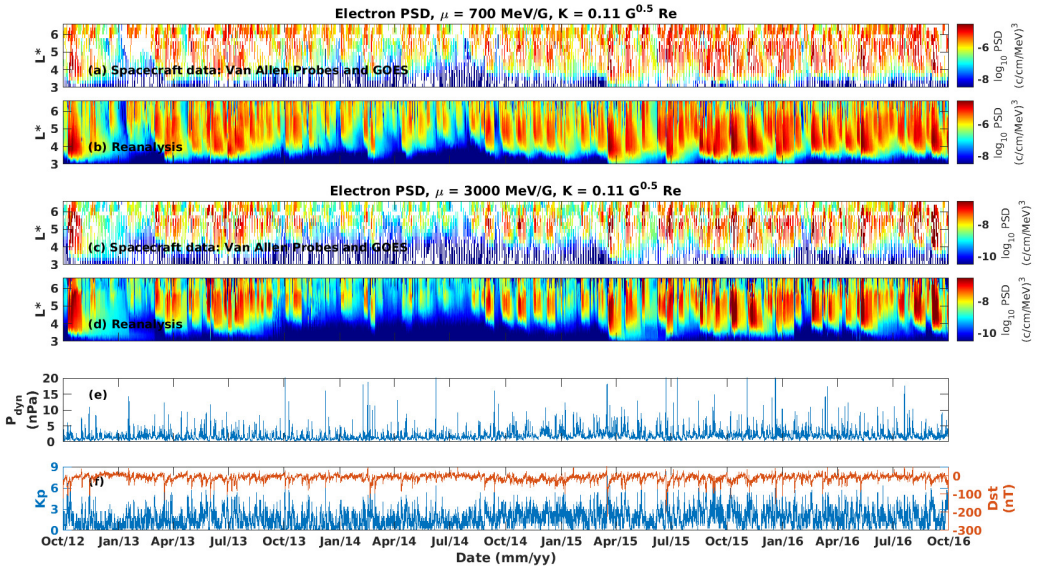

Figure 2. Evolution of electron PSD as a function of L^* and time from 1 October 2012 to 1 October 2016: (a) Van Allen Probes and GOES data, and (b) assimilated radial profile of PSD for $\mu = 700$ MeV G^{-1} and $K = 0.11$ $G^{0.5}$ R_E; (c) and (d) same as (a) and (b) but for $\mu = 3000$ MeV G^{-1} and $K = 0.11$ $G^{0.5}$ R_E; (e) evolution of solar wind dynamic pressure, and (f) geomagnetic activity Kp and Dst indices. The assimilative results of the combined reanalysis of electron PSD in this figure account for 3D diffusion, mixed pitch angle-energy diffusion, scattering by EMIC waves, and magnetopause shadowing (i.e. "full" run).

The reanalysis on panels (b) and (d) exhibit sudden dropouts and buildups of PSD. Figure 2 shows that dropouts in PSD often occur in association with sharp increases of solar wind dynamic pressure (e.g., Shprits et al., 2012; Turner et al., 2012; Ni et al., 2013). It is also worth noting that during the first half of our period under study, particularly between October 2013 and October 2014, geomagnetic activity was much weaker and less PSD enhancements were apparent than during 2015 and 2016.

4 Statistical analysis of loss processes via the innovation vector

In order to understand the loss due to scattering by EMIC waves and magnetopause shadowing in the outer radiation belt, we present plots of the normalized innovation $\mathbf{x}^i$ and the difference of normalized innovations $\Delta\mathbf{x}^i$ (equation 12) for each of our four-year runs and each of our four chosen pairs of adiabatic invariants. We first bin the hourly

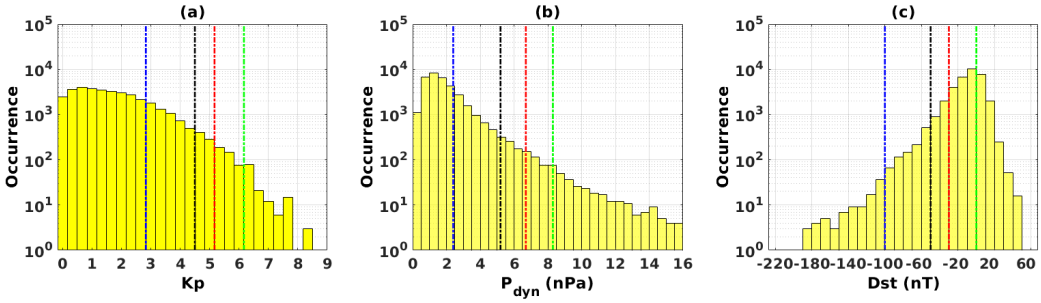

Figure 3. Occurrence of (a) Kp index, (b) solar wind dynamic pressure P_{dyn}, and (c) Dst index. Note that the y-axes are logarithmic. In plots (a) and (b) the blue, black, red, and green dashed lines denote the 75th, 96th, 98th, and 99th percentiles, respectively. In plot (c) the dashed lines indicate Dst values of -100nT, -50 nT, -30 nT, and 0 nT. In plot (b) P_{dyn} is binned each 0.5 nPa, and in plot (c) Dst is binned each 10 nT.

normalized innovation vector according to the Kp index, and compute the average as a function of L^* and Kp. The same procedure is then followed binning the normalized innovation by solar wind dynamic pressure. Figure 3 shows the occurrence of Kp, P_{dyn}, and Dst from 1 October 2012 to 1 October 2016, and the coloured lines indicate different thresholds of geomagnetic activity. Figures A2 and A3 (in the supplementary material) present the distribution of the number of measurements binned by both Kp and P_{dyn}. As expected, the distribution of samples is highly skewed towards low values of Kp index and solar wind dynamic pressure.

4.1 Scattering by EMIC waves

The normalized innovation vector $\mathbf{x}^i$ as a function of L^* and Kp, before (run number 2) and after incorporating EMIC waves (run number 1, i.e. "full") into the model, is shown in the first two rows of Figure 4. Negative values (blue) denote additional loss missing from the radiation belt model, and thus the KF subtracts PSD in order to compensate and match the observations, i.e. our model overestimates the electron PSD. The last row presents the difference $\Delta\mathbf{x}^i$ as defined by equation 12 (namely the second row minus the first row) in which the blue color denotes the area in L^* and Kp where EMIC wave scattering operates and effectively scatters electrons. The positive yellow bins correspond to the intervals, mostly during disturbed times, when the inclusion of EMIC waves

in our model brings more loss than is observed. This may indicate that the parameterization we employ based on solar wind dynamic pressure does not always perform well during periods of high geomagnetic activity. The vertical dashed lines delineating the region of EMIC induced scattering loss are drawn considering a threshold of $\Delta \mathbf{x}^i = 10\%/\text{hr}$.

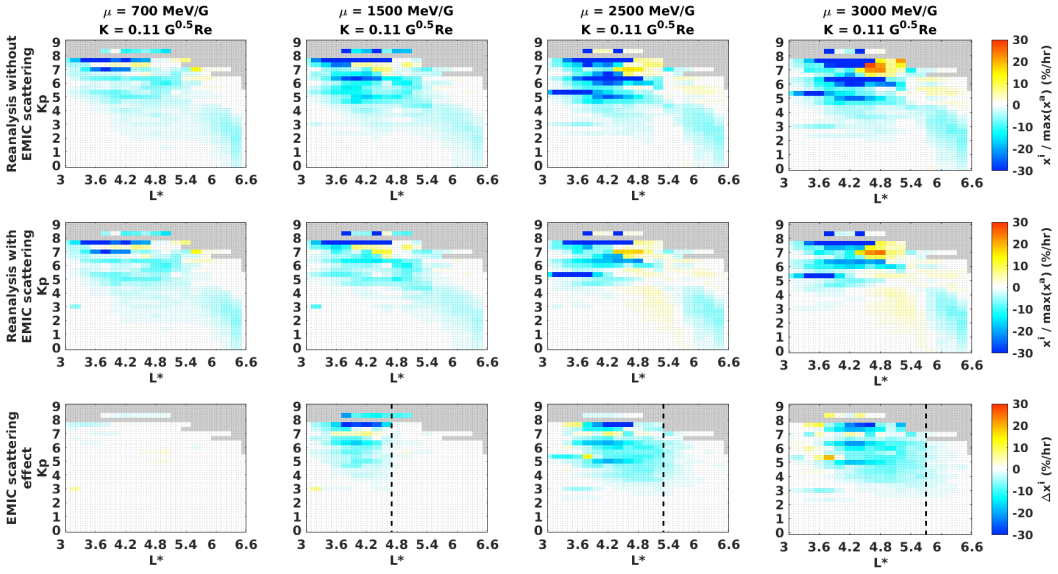

Figure 4. First row: normalized innovation vector $\mathbf{x}^i$ of the reanalysis without EMIC scattering (run number 2); second row: normalized innovation vector $\mathbf{x}^i$ of the "full" run (number 1); third row: difference of innovations $\Delta \mathbf{x}^i$, where the shaded region limited by the dashed line indicates the area where EMIC scattering is effective. The results are binned by L^* and Kp. Each column indicates a different pair of adiabatic invariants (μ, K).

As expected, EMIC waves do not affect the $\mu = 700$ MeV G^{-1} population, whereas they have a much more pronounced effect for higher energy electrons (e.g., Shprits, Subbotin, et al., 2013; Kersten et al., 2014; Usanova et al., 2014; Shprits et al., 2016). The upper extent of the region of loss due to EMIC waves moves from $L^* = 4.6$ (for $\mu = 1500$ MeV G^{-1}), to $L^* = 5.2$ (for $\mu = 2500$ MeV G^{-1}), and further beyond to $L^* = 5.6$ as μ increases to 3000 MeV G^{-1}. In terms of Kp, the scattering effect is evident for $Kp \geq 3$. On average, the loss brought by EMIC waves is between 15%/hr and 30%/hr of the maximum PSD, peaking at $Kp \geq 5$ and between $L^* = 4$ and $L^* = 4.8$.

We also bin $\mathbf{x}^i$ and $\Delta \mathbf{x}^i$ by L^* and P_{dyn} as presented in Figure 5. Similar to the results from Figure 4, including EMIC waves in the model decreases the overestimation

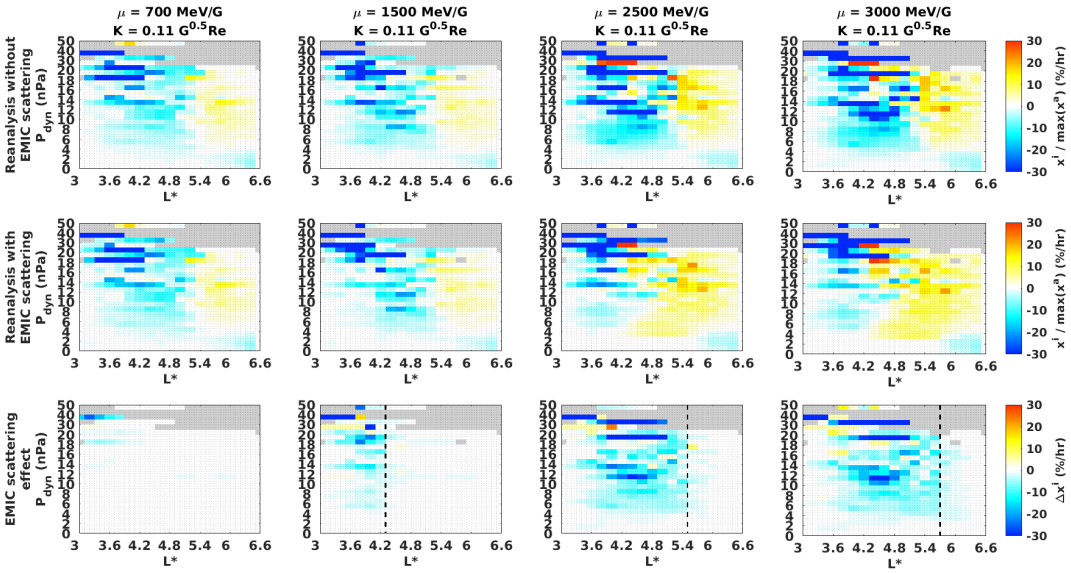

Figure 5. Same format as Figure 4, binning the results by L^* and P_{dyn}. Results are presented in bins of 1 nPa between $P_{dyn} = 0$ and $P_{dyn} = 20$ nPa and 5 nPa between $P_{dyn} = 20$ nPa and $P_{dyn} = 50$ nPa.

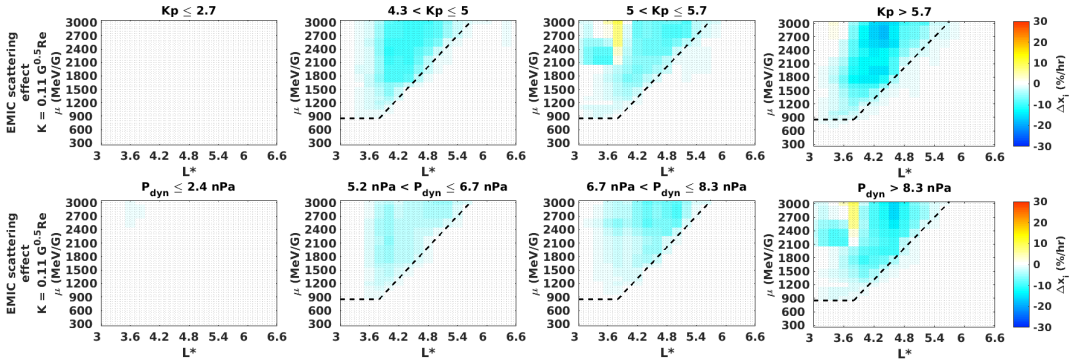

Figure 6. Difference of innovations $\Delta\mathbf{x}^i$ before and after including EMIC waves in the model for different intervals of geomagnetic activity defined by Kp index (first row) and P_{dyn} (second row) as a function of L^* and μ. The shaded region limited by the dashed line indicates the area where EMIC scattering is effective.

of PSD, particularly for higher values of μ between $L^* = 4.2$ and $L^* = 5.6$. The scattering effect of these waves is evident for intervals with $P_{dyn} \geq 2$ nPa, and it exceeds 20% of the maximum PSD for $P_{dyn} \geq 10$ nPa and $4.2 \leq L^* \leq 4.8$. Our choice of binning the innovation by solar wind dynamic pressure follows the previous works from Usanova

et al. (2008) and Usanova et al. (2012) (and references therein), which demonstrated that strong magnetospheric compressions associated with high P_{dyn} may drive EMIC waves, and that the occurrence rate of EMIC activity in the dayside outer magnetosphere is controlled to a large extent by solar wind dynamic pressure.

The top row of figure 6 shows the difference, $\Delta\mathbf{x}^i$, across a range of the first adiabatic invariant extending from $\mu = 300$ MeV G^{-1} ($E_k = 0.87$ MeV at the heart of the outer belt) to $\mu = 3000$ MeV G^{-1}, for both quiet and disturbed geomagnetic conditions as defined by the Kp index. For $Kp \leq 2.7$ (corresponding to the 75th percentile, see the histogram in Figure 3) EMIC waves do not contribute to loss. The next three intervals, defined by the 96th, 98th, and 99th percentiles, and characterizing active times, show that the effect of these waves is confined to a triangular-shaped region defined by $\mu \geq 900$ MeV G^{-1} ($E_k = 1.78$ MeV at the heart of the outer belt) and extending from $L^* = 3.6$ to $L^* = 6$, on average. The loss brought in by EMIC waves increases from $\sim 10\%$/hr of the maximum PSD for Kp between 4.3 and 5 to $\sim 20\%$/hr for $Kp > 5.7$ (equivalent to the 99th percentile), between $L^* = 4.2$ and $L^* = 4.8$. A similar pattern is observed in the second row of Figure 6, where the results are plotted for different intervals of solar wind dynamic pressure. With increase of P_{dyn} and μ, the loss effect due to EMIC waves is enhanced and extends in radial distance from the Earth, maximizing between $L^* = 4$ and $L^* = 4.8$.

4.2 Magnetopause shadowing

An important process in producing fast electron dropouts is magnetopause shadowing coupled with outward radial diffusion (Shprits et al., 2006). We inspect its effect in our four-year reanalysis via the difference of innovations $\Delta\mathbf{x}^i$ when including and not including this process (runs number 1 and 3, respectively), binned according to Kp and P_{dyn}. Figure 7 shows that loss resulting from magnetopause shadowing extends from the outer boundary for $Kp = 3$ down to $L^* = 3.6$ for $Kp > 7$. Therefore, we observe a statistical picture where the loss region extends to lower L^* at a rate of $\sim 0.75\mathrm{R_E}$ per increase of 1 Kp unit. Not surprisingly, the largest values of $\Delta\mathbf{x}^i$, and accordingly, the biggest loss due to magnetopause shadowing ($> 60\%$/hr of the maximum PSD), take place with $Kp \geq 5$ and at $L^* \geq 4.6$. A similar pattern is observed when binning $\Delta\mathbf{x}^i$ by solar wind dynamic pressure (Figure 8). Magnetopause loss starts at $P_{dyn} = 2$ nPa, and they peak (between 50 and 70%/hr of the maximum PSD) when P_{dyn} exceeds 10

nPa at $L^* \geq 4.8$, on average. In both figures, the diagonal dashed lines that define the region of loss correspond to a threshold of $\Delta \mathbf{x}^i = 30\%/\text{hr}$.

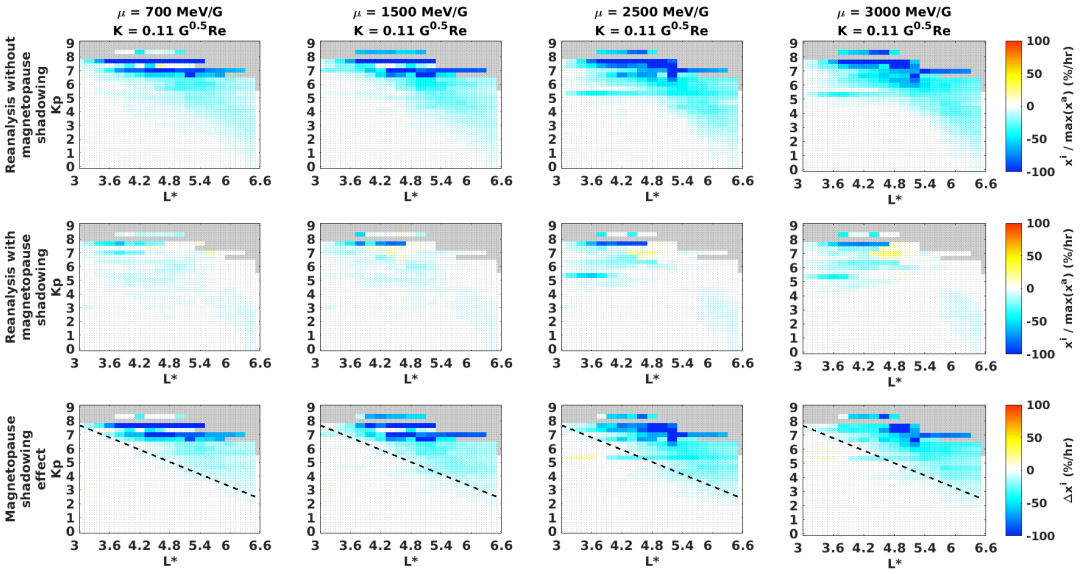

Figure 7. First row: normalized innovation vector $\mathbf{x}^i$ of the reanalysis without magnetopause shadowing (run number 3); second row: normalized innovation vector $\mathbf{x}^i$ of the "full" run (number 1); third row: difference of innovations $\Delta \mathbf{x}^i$, where the shaded region indicates the region where magnetopause shadowing operates. The results are binned by L^* and Kp. Each column indicates a different pair of adiabatic invariants (μ, K).

Figure 9 shows that as geomagnetic activity increases from quiet to disturbed times, loss moves inward affecting all values of μ from 300 to 3000 MeV G^{-1}. The effect is more pronounced for electrons with values of the invariant $\mu \geq 1500$ MeV G^{-1} ($\Delta \mathbf{x}^i$ between 30%/hr and 50%/hr at $L^* \geq 5$) than for those with lower μ ($\Delta \mathbf{x}^i \sim 15\%/\text{hr}$, on average), as the former drift faster, and thus, are depleted more quickly than less energetic ones. Likewise, increases in solar wind dynamic pressure also move the loss region due to magnetopause shadowing towards low L^*.

Lastly, we analyze our results by binning $\Delta \mathbf{x}^i$ (Figure 10) according to the geomagnetic activity Dst index (the corresponding histogram is shown in Figure 3 and the distribution of measurements binned by Dst is presented in Figure A4). For electrons with $\mu = 700$ MeV G^{-1} loss due to magnetopause shadowing exceed 50%/hr of the maxi-

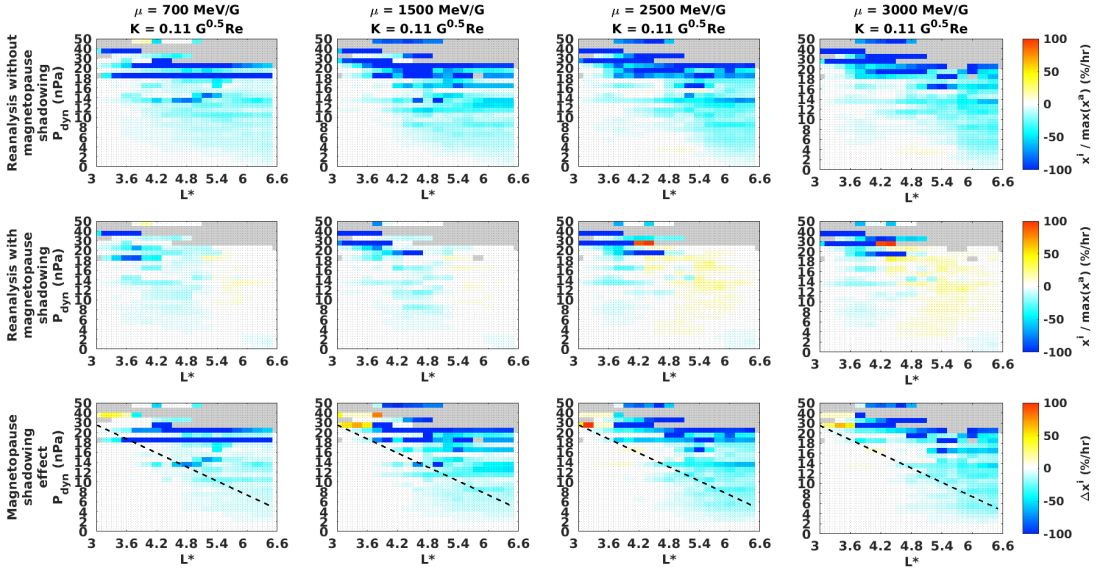

Figure 8. Same format as Figure 7, binning the results by L^* and P_{dyn}.

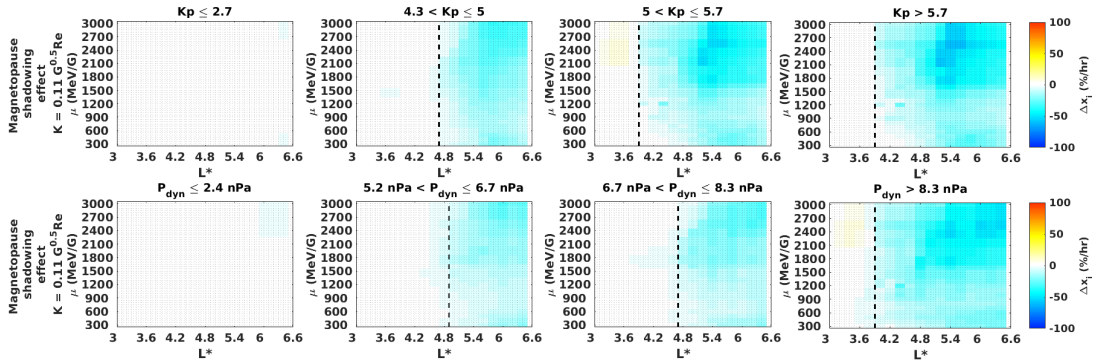

Figure 9. Difference of innovations $\Delta \mathbf{x}^i$ before and after magnetopause shadowing in the model for different intervals of geomagnetic activity defined by Kp index (first row) and P_{dyn} (second row) as a function of L^* and μ.

mum PSD for $Dst < -100$ nT, whereas for those with $\mu = 3000$ MeV G^{-1} such level of loss is already evident at $Dst = -75$ nT. In other words, as μ increases, less geomagnetic activity, as described by Dst, is required to observe the same percentage loss to the magnetopause. It is also worth noting that, irrespective of the particle's energy, loss due to magnetopause shadowing extends down to $L^* = 4.4$ during times with -100 nT $< Dst \leq -50$ nT and even below to $L^* = 3.6$ when $Dst < -100$ nT.

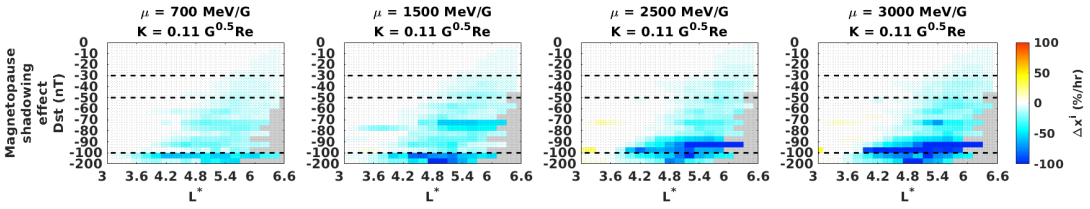

Figure 10. Difference of innovations $\Delta\mathbf{x}^i$ binned by L^* and Dst. The dashed lines indicate thresholds of -100 nT, -50 nT, and -30 nT. Results are presented in bins of 5 nT between $Dst = 0$ and $Dst = -100$ nT and 50 nT between $Dst = -100$ nT and $Dst = -200$ nT.

4.3 Comparison of electron PSD loss mechanisms

The previous sections have quantitatively determined via data assimilation the effect of EMIC scattering and magnetopause shadowing in the outer radiation belt. Here we analyse both processes simultaneously and compare the magnitude and the spatial extent (in L^*) of the loss induced by them. Figure 11 presents the difference $\Delta\mathbf{x}^i$ as a function of radial distance averaged over the following levels of geomagnetic activity during our four-year period under study: -30 nT $< Dst \leq 0$ nT, -50 nT $< Dst \leq -30$ nT, and $Dst \leq -50$ nT. The minima of these curves are interpreted as the maximum loss achieved by either of the mechanisms. In accordance with the above-mentioned results, EMIC waves bring fewer loss than magnetopause shadowing. Loss due to EMIC waves is mostly seen at L^* between 3.6 and 4.6, whereas loss due to magnetopause shadowing is mainly evident at higher radial distances ($L^* \geq 4.8$).

The mimimum values of each curve of Figure 11, as well as their corresponding L^* locations, are plotted in panels (a) and (b) of Figure 12. For the lowermost geomagnetic activity level, with Dst between -30 nT and 0 nT, only loss due to magnetopause shadowing is apparent, fluctuating between 2%/hr and 4%/hr of the maximum PSD at $L^* = 6.4$. As Dst decreases between -50 nT and -30 nT, EMIC waves scatter electrons with $\mu > 1000$ MeV G^{-1}. Such loss reaches, at most, 5%/hr for the highest μ values, and is observed from $L^* = 3.6$ to $L^* = 4.8$. At the same geomagnetic activity level, magnetopause shadowing depletes electrons amounting from 10%/hr to 25%/hr of the maximum PSD between $L^* = 5.8$ and $L^* = 6$. For the intervals with $Dst \leq -50$ nT, the maximum EMIC induced scattering ($\Delta\mathbf{x}^i \leq 10$%/hr) occurs at $3.4 \leq L^* \leq 4.2$, and

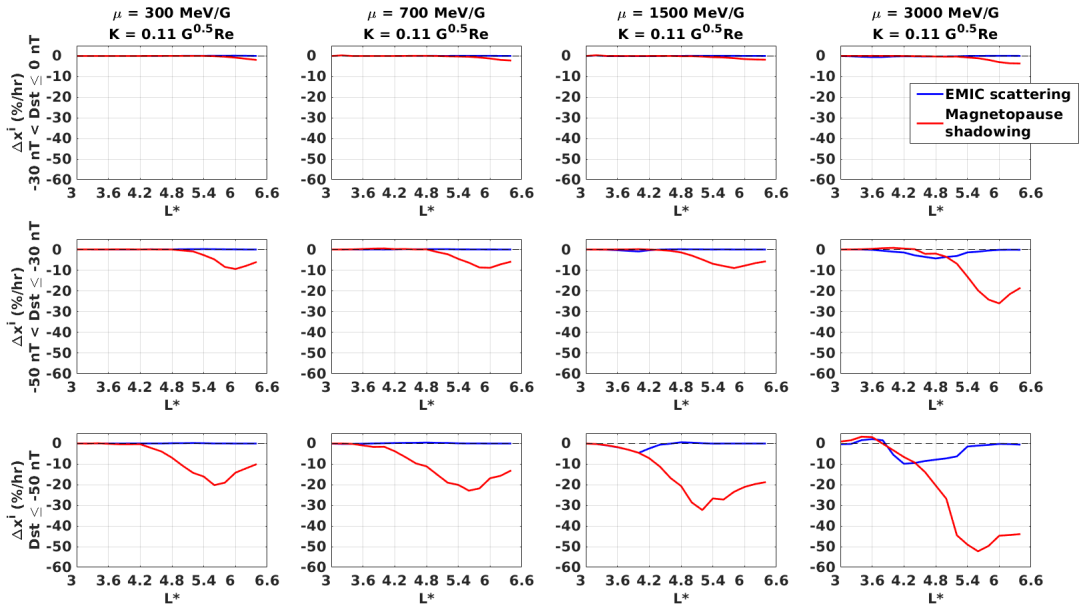

Figure 11. Difference of innovations $\Delta\mathbf{x}^i$ binned by L^* for different intervals of geomagnetic activity defined by Dst index for the indicated pairs of adiabatic invariants (μ, K). Blue (red) lines denote loss due to EMIC scattering (magnetopause shadowing).

it clearly intensifies with increasing μ. More dramatic loss is introduced by magnetopause shadowing, ranging on average between 20%/hr and 50%/hr, at L^* between 5.2 and 5.6.

Besides investigating the value and L^* of the maximum PSD loss, we also determine the location at which loss due to magnetopause shadowing starts dominating over that due to EMIC wave scattering, by finding the crossing between the red and blue curves in Figure 11. The corresponding L^* values are plotted in panel (c) of Figure 12. This intersection is clearly energy-dependent, and for Dst between -50 nT and -30 nT, it extends from $L^* = 4.1$ ($\mu = 1000$ MeV G^{-1}) to $L^* = 5.2$ ($\mu = 3000$ MeV G^{-1}), i.e. out of the two loss processes inspected, EMIC waves are the main scattering agent below such location, whereas magnetopause shadowing plays a dominant role above it. For more disturbed times, with $Dst \leq -50$ nT, this boundary moves inwards and fluctuates between $L^* = 3.5$ and $L^* = 4.4$. Nevertheless, it is worth noting that EMIC waves (magnetopause shadowing) may deplete electrons above (below) such location. As an example, for $Dst \leq -50$ nT and $\mu = 3000$ MeV G^{-1}, EMIC waves produce loss beyond the intersection at $L^* = 4.4$, extending out to $L^* = 5$. Conversely, loss due to magnetopause shadowing is already seen at $L^* = 4$.

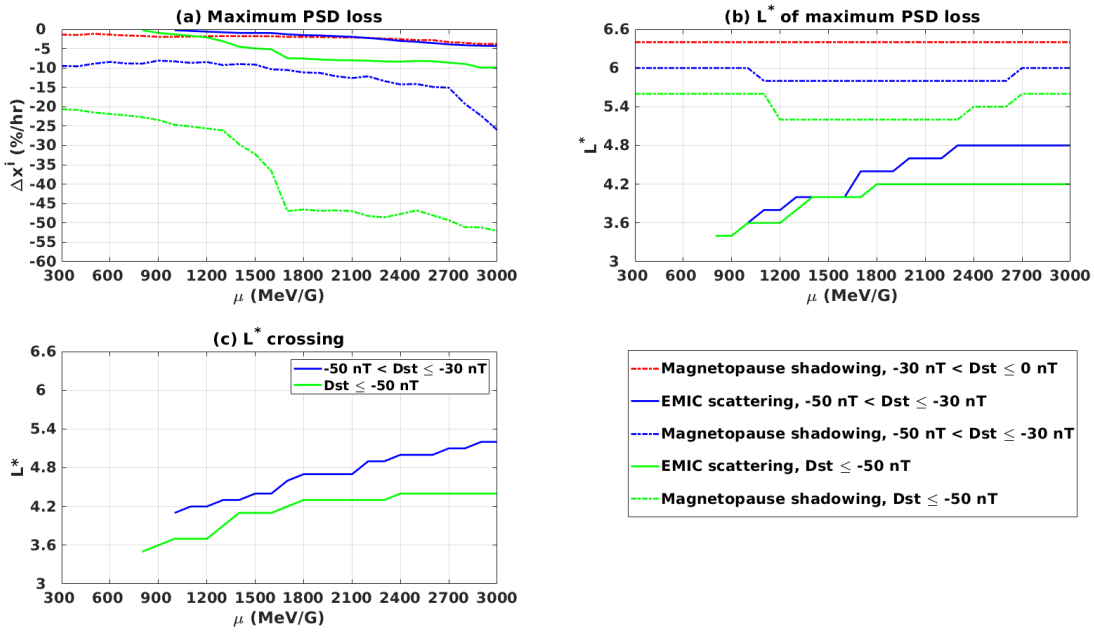

Figure 12. (a) Maximum loss (as defined by $\Delta \mathbf{x}^i$) due to EMIC scattering and magnetopause shadowing for the indicated levels of geomagnetic activity; (b) L^* location corresponding to the maximum loss; (c) L^* boundary separating two distinct mechanisms of electron PSD loss.

5 Discussion

This work employs four-years of spacecraft data which allows us to statistically quantify the effect of both loss processes over different levels of geomagnetic activity. We show that scattering by EMIC waves induces loss from $L^* = 3.6$ to $L^* = 5.6$, particularly between $L^* = 4$ and $L^* = 4.8$ during the most disturbed times. The resulting depletion amounts to between 10%/hr to 30%/hr of the maximum PSD. The effect of EMIC waves is seen starting from $\mu = 900$ MeV G^{-1}, and is energy-dependent, with higher energy electrons being affected the most over a broader range of L^*. Our findings are consistent with previous observational and modelling studies (e.g., Usanova et al., 2014; Shprits et al., 2016; Drozdov, Shprits, Usanova, et al., 2017; Xiang et al., 2017), and validate the employed wave model, since we are able to reproduce the behaviour of EMIC waves and the dynamics of the ultrarelativistic electron population.

Loss due to magnetopause shadowing is the strongest between $L^* = 5$ and $L^* = 6.6$. Nevertheless, the depletion of electron PSD may extend further below $L^* = 4$ and reach between 50%/hr and 70%/hr of the maximum PSD, either for large values of ge-

omagnetic indices or for enhanced solar wind dynamic pressure. This is in accordance with e.g. Shprits et al. (2012), who reconstructed a depletion of the radiation belt PSD down to $L^* = 3$, based on data assimilation, for a very high value of P_{dyn} around 50 nPa. Similar conclusions on the correlation between electron PSD dropout events and solar wind dynamic pressure pulses were reached by Ni et al. (2013), based on a one-year reanalysis survey of multisatellite data. Such sharp increases of P_{dyn} clearly result in the compression of the magnetopause and the removal of electrons originally on closed drift orbits, with the most energetic populations affected to a larger extent. Statistically, for the range of μ values considered in this study, we find that magnetopause shadowing tends to deplete more electrons than EMIC wave interactions during disturbed times.

Based on our results we identify a μ- and geomagnetic activity-dependent boundary fluctuating between $L^* = 3.5$ and $L^* = 5.2$ defining two regions in space where these two distinct loss mechanisms are mostly effective. EMIC induced scattering dominates below the boundary, whereas magnetopause shadowing coupled with outward radial diffusion is active above it. Turner, Angelopoulos, Morley, et al. (2014) suggested this boundary to be located at $L^* \sim 4$. Yu et al. (2013) found it to be around $L^* \sim 5$, above which more than 90%/hr of the total loss is due to magnetopause shadowing together with outward radial diffusion, and below which only 60%/hr can be explained by this coupled mechanism. Dropouts, however, can encompass the entire outer radiation belt, and either mechanism can induce loss beyond the above-mentioned boundary. In other words, magnetopause shadowing can deplete electrons below it, and EMIC waves can efficiently scatter electrons beyond it, in particular during times of enhanced geomagnetic activity. A similar conclusion with a boundary identified around $L^* \sim 4$ was reached by Xiang et al. (2017) based on an investigation of three dropouts as observed by Van Allen Probes.

Our statistical study relying on four years of data has shown that, in general, loss due to magnetopause shadowing tends to exceed loss produced by EMIC scattering. Nevertheless, this is not always the case, as during disturbed conditions (i.e. geomagnetic storms) the effect of EMIC waves can be comparable, or even exceed, the effect of magnetopause shadowing. Figures 13 and 14 show two of these events, which correspond to intense storms following the classification of Gonzalez et al. (1994). The maximum depletion due to both EMIC waves and magnetopause shadowing (between 10%/hr and 20%/hr of the maximum PSD) is observed during the main phase of each storm, with

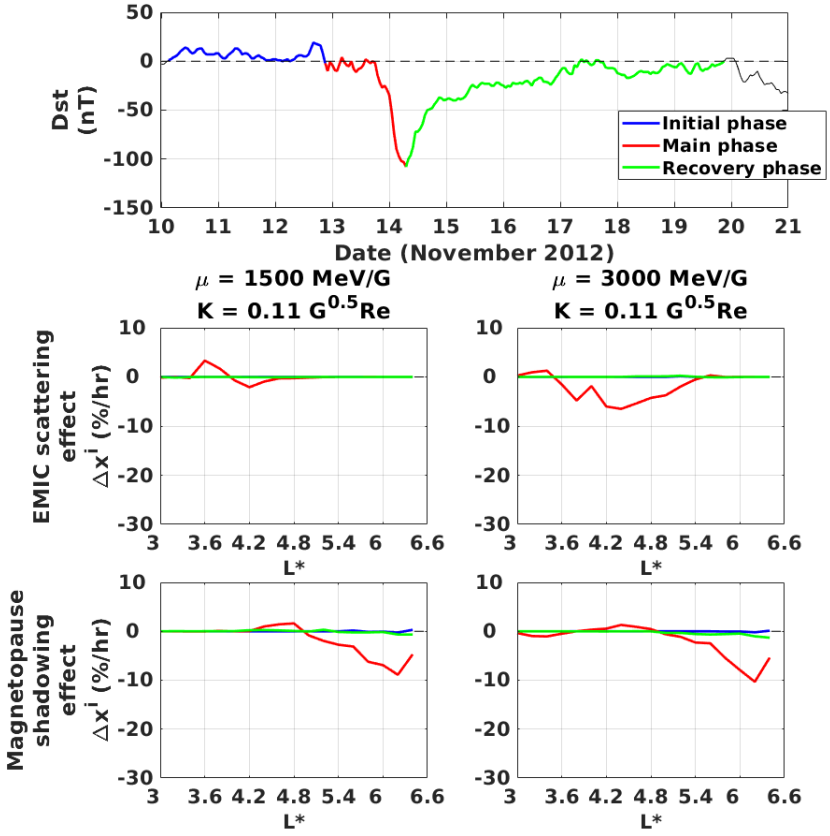

Figure 13. First row: evolution of Dst index for the geomagnetic storm with $Dst_{min} = -108$ nT on 14 November 2012 07 UT. The initial, main, and recovery phases are highlighted in blue, red, and green, respectively. Second row: difference of innovations $\Delta \mathbf{x}^i$ binned by L^* denoting losses due to scattering by EMIC waves for the indicated pairs adiabatic invariants (μ, K) during different phases of the storm. Third row: same as second row, for magnetopause shadowing.

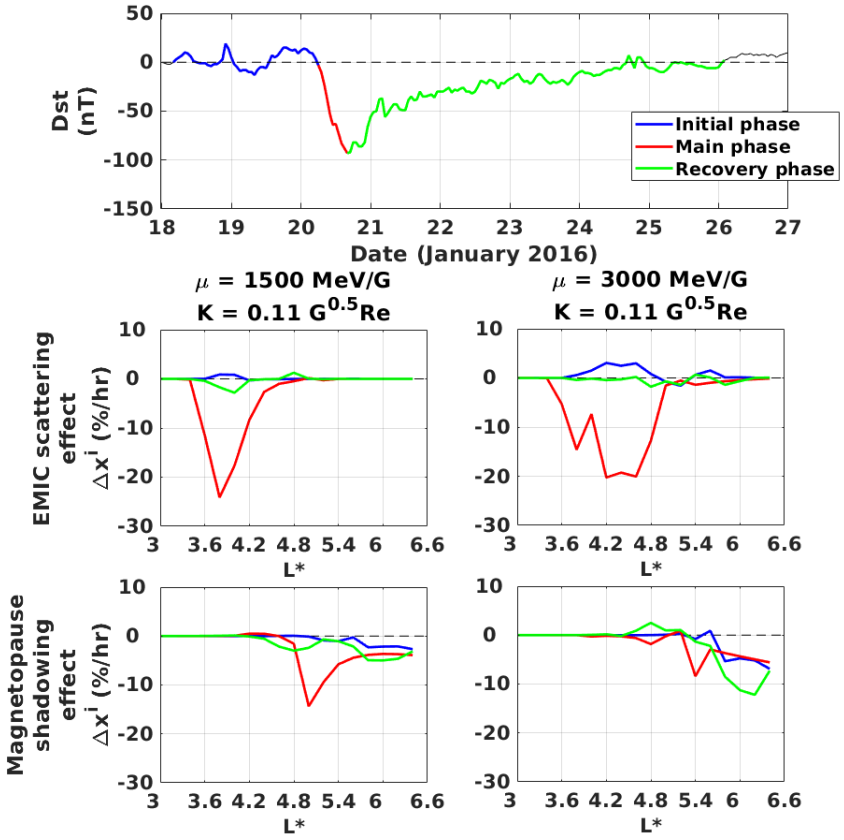

Figure 14. Same as Figure 13, for the storm with $Dst_{min} = -93$ nT on 20 January 2016 16 UT.

smaller contributions during the initial phase and the beginning of the recovery phase. In these events, loss due to EMIC waves dominates in the heart of the outer radiation belt and is within the same order of magnitude as loss produced by magnetopause shadowing, demonstrating that EMIC waves play an indispensable role in the dynamics of the ultrarelativistic electron population.

The effects of scattering by EMIC waves and magnetopause shadowing have been studied individually in the current work, i.e. only one process was excluded from the model at a time. However, these two mechanisms can act simultaneously and complement each other in driving the dynamics of the outer belt. Magnetopause shadowing and the consequent outward radial diffusion develop negative PSD gradients at higher L shells (e.g., Turner et al., 2012), while localized and fast loss driven by EMIC waves produces deepening minimums in PSD around $L^* = 3.5$ to $L^* = 4.5$ (e.g., Aseev et al., 2017; Shprits et al., 2017), and therefore can influence the rate of outward diffusion. The combination of both processes results in efficient dropouts of radiation belt electrons, creating several localized peaks in PSD. Moreover, EMIC wave scattering is fast at low pitch angles and significantly slower at high pitch angles, (e.g., Usanova et al., 2014; Drozdov, Shprits, Usanova, et al., 2017). LCDS location is also pitch angle (or K) dependent (e.g., Albert et al., 2018) and magnetopause shadowing affects mainly high pitch angles (e.g., Roederer, 1967; West et al., 1972). As a result, both mechanisms can remove together a broad range of particles. This can irreversibly alter the content of the outer belt and can lead to almost total depletion of the pre-existing electron population. Future work will focus on estimating the K dependence of scattering by EMIC waves and magnetopause shadowing via the analysis of the innovation vector.

After adding EMIC waves and magnetopause shadowing in our model (i.e. performing the "full" run) a region of positive innovation (in yellow and red) remains at $L^* > 4.2$ and $Kp > 6$. This underestimation of electron PSD could be due to the fact that our calculation of the LCDS, based on the IRBEM library, does not account for bifurcating field lines (Albert et al., 2018), thus yielding a LCDS that is too close to Earth. As a result, electron PSD is depleted in excess. Another explanation for this underestimation of PSD is related to the electric field induced by the compression of the magnetopause. Such electric field might mitigate some of the ensuing loss by radially transporting the electron population inwards (Michael Schulz, personal communication, May 2019).

The technique we have presented in this study can be applied to other geophysical systems where the relative contribution of specific mechanisms needs to be quantified. This comes with several caveats, however. First of all, while our technique relies on spacecraft observations, our findings are not completely independent of the assumptions of the model, such as the times when EMIC waves operate or the location of the LCDS. Second, the metric we have introduced, $\Delta\mathbf{x}^i$, does not indicate the actual number of electrons lost (an integration would be necessary), but rather expresses the loss in each time step as a function of the hourly maximum PSD. In this regard, we have chosen our normalization factor to be the maximum value of assimilated PSD over all L^*, rather than the current state at each individual L^*, to avoid division by rather small values, which would have yielded large percentage differences at some locations. Lastly, in our case, errors in the model may arise, e.g. from the employed wave parameterizations or the dynamic pressure threshold used to turn on EMIC waves in the model, and in turn, may affect the reconstructed electron PSD and the innovation vector. Nevertheless, the difference of innovations $\Delta\mathbf{x}^i$ can be used to indicate when discrepancies between predictions and observations arise and to pinpoint possible sources of error in the model. In our current study, values of $\Delta\mathbf{x}^i$ are mainly negative and hence, indicate that loss by EMIC waves and magnetopause shadowing decrease the modeled PSD and generally bring the model output closer to observations.

6 Conclusions

In this paper we perform four-year reanalysis of the outer electron radiation belt by assimilating Van Allen Probes and GOES electron PSD measurements into our VERB-3D code. We study the innovation vector to characterize the effect of two distinct processes, namely scattering by EMIC waves and magnetopause shadowing, identifying where (in L^*) and under which conditions (as described by geomagnetic indices Kp and Dst as well as solar wind parameter P_{dyn}) they operate. In comparison to previous studies, our novel approach accounts and corrects for limited data coverage. We quantify the loss produced by these mechanisms through a comparison of the innovation before and after their inclusion in the model, and we also explore the μ dependence (from 300 to 3000 MeV G^{-1}) of both processes.

We find that EMIC waves mainly scatter electrons with $\mu \geq 900$ MeV G^{-1} between $L^* = 4$ and $L^* = 4.8$, and the ensuing depletion may reach between 10%/hr to

30%/hr of the maximum PSD under disturbed geomagnetic conditions. Magnetopause shadowing is shown to be mostly effective from $L^* = 5$ to $L^* = 6.6$ and the induced loss may amount up to between 50%/hr and 70%/hr of the maximum PSD, affecting all electrons with μ values from 300 to 3000 MeV G^{-1}. We also identify an energy- and geomagnetic activity-dependent boundary located between $L^* = 3.5$ and $L^* = 5.2$ separating both mechanisms. Scattering by EMIC waves is active below it, while magnetopause shadowing dominates above it.

Future studies will be aimed towards extending our DA methodology and innovation vector analysis to quantify and assess the contribution of other processes to the dynamical evolution of electron PSD, such as pitch angle scattering by plasmaspheric hiss or energy diffusion by chorus waves. Same methodology can be also applied to the analysis of the ring current dynamics. Furthermore, the role of scattering by EMIC waves and magnetopause shadowing will be inspected in detail for selected events, such as the 110 geomagnetic storms identified by Turner et al. (2019) during the Van Allen Probes era, in order to determine the percentage of dropout events dominated by either mechanism. Moreover, our framework can also be employed to assimilate measurements from the last three years of Van Allen Probes (October 2016 to October 2019) and from ongoing missions such as Arase (Miyoshi et al., 2018). All these efforts will be ultimately directed towards achieving a better understanding of the dominant mechanisms during radiation belt enhancements and dropouts.

Appendix A Supplementary material

Acknowledgments

The authors acknowledge use of NASA/GSFC's Space Physics Data Facility's OMNIWeb service, and OMNI data (https://omniweb.gsfc.nasa.gov/). The Kp index was provided by GFZ Potsdam (https://www.gfz-potsdam.de/kp-index/). The authors are grateful to the RBSP-ECT team for the provision of Van Allen Probes observations (http://rbsp-ect.lanl.gov/). The authors thank the developers of the IRBEM library which was adapted for use in the current study (http://irbem.sourceforge.net). We thank Michael Schulz for stimulating discussions and Adam Kellerman for the development of the initial codes. This research has been funded by Deutsche Forschungsgemeinschaft (DFG) through grant CRC 1294 "Data Assimilation", Project B06 "Novel methods for the 3D reconstruction

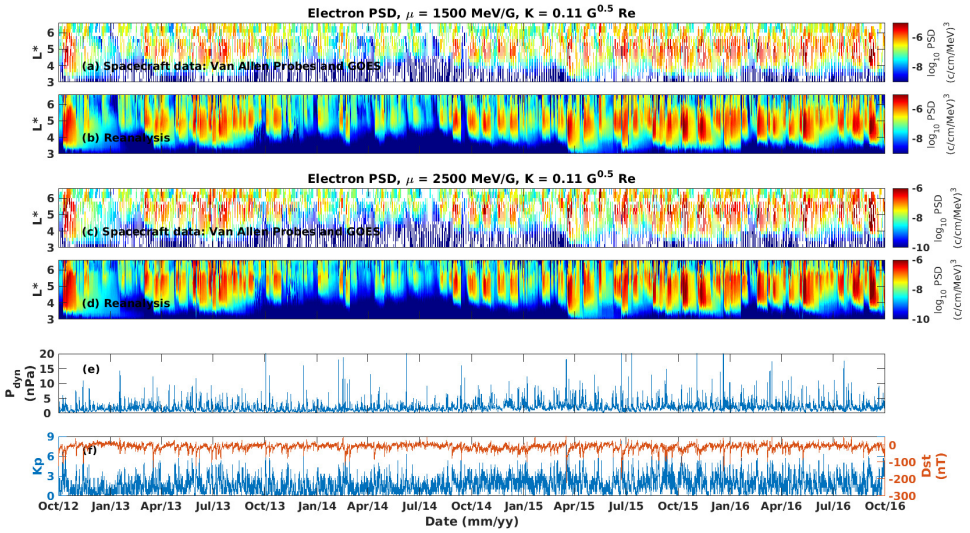

Figure A1. Evolution of electron PSD as a function of L^* and time from 1 October 2012 to 1 October 2016: (a) Van Allen Probes and GOES data, and (b) assimilated radial profile of PSD for $\mu = 1500$ MeV G^{-1} and $K = 0.11$ $G^{0.5}$ R_E; (c) and (d) same as (a) and (b) but for $\mu = 2500$ MeV G^{-1} and $K = 0.11$ $G^{0.5}$ R_E; (e) evolution of solar wind dynamic pressure, and (f) geomagnetic activity Kp and Dst indices. The assimilative results of the combined reanalysis of electron PSD in this figure account for 3D diffusion, mixed pitch angle-energy diffusion, scattering by EMIC waves, and magnetopause shadowing (i.e. "full" run).

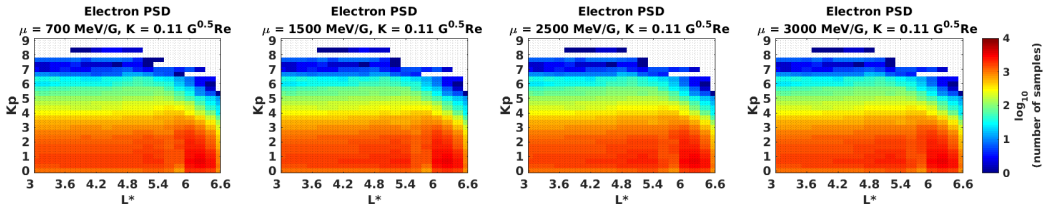

Figure A2. Distribution of the number of satellite observations employed in the reanalysis of PSD binned by L^* and Kp for the indicated pair of adiabatic invariants μ and K.

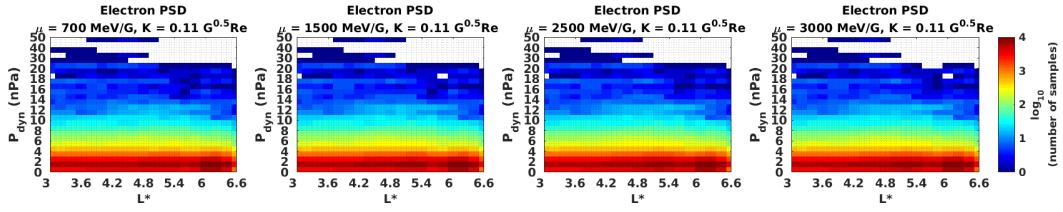

Figure A3. Distribution of the number of satellite observations employed in the reanalysis of PSD binned by L^* and P_{dyn} for the indicated pair of adiabatic invariants μ and K.

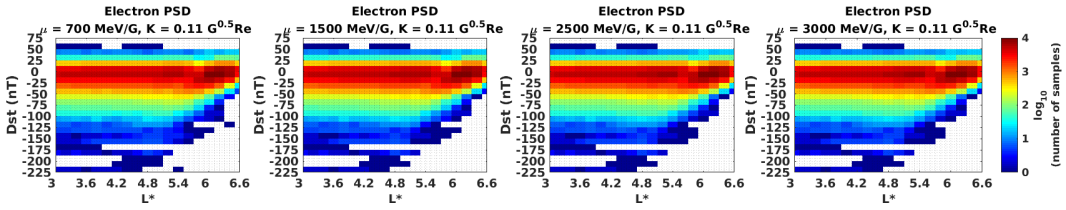

Figure A4. Distribution of the number of satellite observations employed in the reanalysis of PSD binned in L^* and Dst for the indicated pair of adiabatic invariants μ and K.

of the dynamic evolution of the Van Allen belts using multiple satellite measurements" and the Helmholtz Association Recruiting Initiative.

References

Albert, J., Selesnick, R., Morley, S., Henderson, M., & Kellerman, A. (2018). Calculation of last closed drift shells for the 2013 gem radiation belt challenge events. *Journal of Geophysical Research: Space Physics*, *123*(11), 9597–9611.

Aseev, N., Shprits, Y., Drozdov, A., Kellerman, A., Usanova, M., Wang, D., & Zhelavskaya, I. (2017). Signatures of ultrarelativistic electron loss in the heart of the outer radiation belt measured by Van Allen Probes. *Journal of Geophysical Research: Space Physics*, *122*(10), 10–102.

Baker, D., Kanekal, S., Hoxie, V., Batiste, S., Bolton, M., Li, X., ... others (2012). The Relativistic Electron-Proton Telescope (REPT) instrument on board the Radiation Belt Storm Probes (RBSP) spacecraft: Characterization of Earth's radiation belt high-energy particle populations. In *The van allen probes mission* (pp. 337–381). Springer.

Blake, J., Carranza, P., Claudepierre, S., Clemmons, J., Crain, W., Dotan, Y., ... others (2013). The magnetic electron ion spectrometer (MagEIS) instruments aboard the radiation belt storm probes (RBSP) spacecraft. In *The van allen probes mission* (pp. 383–421). Springer.

Bortnik, J., Thorne, R., O'Brien, T., Green, J., Strangeway, R., Shprits, Y., & Baker, D. (2006). Observation of two distinct, rapid loss mechanisms during the 20 November 2003 radiation belt dropout event. *Journal of Geophysical Research: Space Physics*, *111*(A12).

Boscher, D., Bourdarie, S., O'Brien, P., & Guild, T. (2012). *Irbem-lib library.*

Brautigam, D., & Albert, J. (2000). Radial diffusion analysis of outer radiation belt electrons during the October 9, 1990, magnetic storm. *Journal of Geophysical Research: Space Physics*, *105*(A1), 291–309.

Carpenter, D., & Anderson, R. (1992). An ISEE/whistler model of equatorial electron density in the magnetosphere. *Journal of Geophysical Research: Space Physics*, *97*(A2), 1097–1108.

Cervantes, S., Shprits, Y., Aseev, N., Drozdov, A., Castillo, A., & Stolle, C. (2020). Identifying radiation belt electron source and loss processes by assimilating spacecraft data in a three-dimensional diffusion model. *Journal of Geophysical Research: Space Physics*, *125*(1).

Daae, M., Shprits, Y., Ni, B., Koller, J., Kondrashov, D., & Chen, Y. (2011). Reanalysis of radiation belt electron phase space density using various boundary conditions and loss models. *Advances in Space Research*, *48*(8), 1327–1334.

Drozdov, A., Shprits, Y., Aseev, N., Kellerman, A., & Reeves, G. D. (2017). Dependence of radiation belt simulations to assumed radial diffusion rates tested for two empirical models of radial transport. *Space Weather*, *15*(1), 150–162.

Drozdov, A., Shprits, Y., Usanova, M., Aseev, N., Kellerman, A., & Zhu, H. (2017). EMIC wave parameterization in the long-term VERB code simulation. *Journal of Geophysical Research: Space Physics*, *122*(8), 8488–8501.

Evensen, G. (1994). Sequential data assimilation with a nonlinear quasi-geostrophic model using Monte Carlo methods to forecast error statistics. *Journal of Geophysical Research: Oceans*, *99*(C5), 10143–10162.

Friedel, R., Reeves, G., & Obara, T. (2002). Relativistic electron dynamics in the inner magnetosphere — A review. *Journal of Atmospheric and Solar-Terrestrial Physics*, *64*(2), 265–282.

Gonzalez, W., Joselyn, J.-A., Kamide, Y., Kroehl, H. W., Rostoker, G., Tsurutani, B., & Vasyliunas, V. (1994). What is a geomagnetic storm? *Journal of Geophysical Research: Space Physics*, *99*(A4), 5771–5792.

Green, J., Onsager, T., O'Brien, T., & Baker, D. (2004). Testing loss mechanisms capable of rapidly depleting relativistic electron flux in the Earth's outer radiation belt. *Journal of Geophysical Research: Space Physics*, *109*(A12).

Hanser, F. (2011). *EPS/HEPAD calibration and data handbook (Tech. Rep. GOESN-ENG-048D). Carlisle, MA: Assurance Technology Corporation.*

Horne, R., Meredith, N., Thorne, R., Heynderickx, D., Iles, R., & Anderson, R. (2003). Evolution of energetic electron pitch angle distributions during storm time electron acceleration to megaelectronvolt energies. *Journal of Geophysical Research: Space Physics*, *108*(A1), SMP–11.

Jazwinski, A. (1970). *Stochastic and Filtering Theory. Mathematics in Sciences and Engineering Series, Series 64*. Academic Press, New.

Kalman, R. (1960). A new approach to linear filtering and prediction problems. *Journal of basic Engineering*, *82*(1), 35–45.

Kellerman, A., Shprits, Y., Kondrashov, D., Subbotin, D., Makarevich, R., Donovan, E., & Nagai, T. (2014). Three-dimensional data assimilation and reanalysis of radiation belt electrons: Observations of a four-zone structure using five spacecraft and the VERB code. *Journal of Geophysical Research: Space Physics*, *119*(11), 8764–8783.

Kersten, T., Horne, R., Glauert, S., Meredith, N., Fraser, B., & Grew, R. (2014). Electron losses from the radiation belts caused by EMIC waves. *Journal of Geophysical Research: Space Physics*, *119*(11), 8820–8837.

Kim, H., & Chan, A. (1997). Fully adiabatic changes in storm time relativistic electron fluxes. *Journal of Geophysical Research: Space Physics*, *102*(A10), 22107–22116.

Kim, K., Lee, D., Kim, H., Lyons, L., Lee, E., Öztürk, M., & Choi, C. (2008). Numerical calculations of relativistic electron drift loss effect. *Journal of Geophysical Research: Space Physics*, *113*(A9).

Koller, J., Chen, Y., Reeves, G., Friedel, R., Cayton, T., & Vrugt, J. (2007). Identifying the radiation belt source region by data assimilation. *Journal of Geophysical Research: Space Physics*, *112*(A6).

Lenchek, A., Singer, S., & Wentworth, R. (1961). Geomagnetically trapped electrons from cosmic ray albedo neutrons. *Journal of Geophysical Research*, *66*(12), 4027–4046.

Lyons, L., Thorne, R., & Kennel, C. (1972). Pitch-angle diffusion of radiation belt electrons within the plasmasphere. *Journal of Geophysical Research*, *77*(19), 3455–3474.

Mauk, B., Fox, N. J., Kanekal, S., Kessel, R., Sibeck, D., & Ukhorskiy, A. (2012). Science objectives and rationale for the Radiation Belt Storm Probes mission.

679 In *The van allen probes mission* (pp. 3–27). Springer.

680 McAdams, K., & Reeves, G. (2001). Non-adiabatic response of relativistic radiation
681 belt electrons to GEM magnetic storms. *Geophysical research letters*, *28*(9),
682 1879–1882.

683 Meredith, N., Horne, R., Kersten, T., Fraser, B., & Grew, R. (2014). Global mor-
684 phology and spectral properties of EMIC waves derived from CRRES observa-
685 tions. *Journal of Geophysical Research: Space Physics*, *119*(7), 5328–5342.

686 Millan, R., & Baker, D. (2012). Acceleration of particles to high energies in Earth's
687 radiation belts. *Space Science Reviews*, *173*(1-4), 103–131.

688 Millan, R., Lin, R., Smith, D., & McCarthy, M. (2007). Observation of relativistic
689 electron precipitation during a rapid decrease of trapped relativistic electron
690 flux. *Geophysical research letters*, *34*(10).

691 Miyoshi, Y., Shinohara, I., Takashima, T., Asamura, K., Higashio, N., Mitani, T., ...
692 others (2018). Geospace exploration project ERG. *Earth, Planets and Space*,
693 *70*(1), 101.

694 Morley, S., Friedel, R., Cayton, T., & Noveroske, E. (2010). A rapid, global and
695 prolonged electron radiation belt dropout observed with the Global Positioning
696 System constellation. *Geophysical Research Letters*, *37*(6).

697 Ni, B., Shprits, Y., Friedel, R., Thorne, R., Daae, M., & Chen, Y. (2013). Responses
698 of Earth's radiation belts to solar wind dynamic pressure variations in 2002
699 analyzed using multisatellite data and Kalman filtering. *Journal of Geophysical*
700 *Research: Space Physics*, *118*(7), 4400–4414.

701 Ohtani, S., Miyoshi, Y., Singer, H., & Weygand, J. (2009). On the loss of relativistic
702 electrons at geosynchronous altitude: Its dependence on magnetic configura-
703 tions and external conditions. *Journal of Geophysical Research: Space Physics*,
704 *114*(A1).

705 Onsager, T., Grubb, R., Kunches, J., Matheson, L., Speich, D., Zwickl, R., & Sauer,
706 H. (1996). Operational uses of the GOES energetic particle detectors. In
707 *Goes-8 and beyond* (Vol. 2812, pp. 281–291).

708 Orlova, K., & Shprits, Y. (2014). Model of lifetimes of the outer radiation belt elec-
709 trons in a realistic magnetic field using realistic chorus wave parameters. *Jour-*
710 *nal of Geophysical Research: Space Physics*, *119*(2), 770–780.

711 Orlova, K., Spasojevic, M., & Shprits, Y. (2014). Activity-dependent global model

of electron loss inside the plasmasphere. *Geophysical Research Letters*, *41*(11), 3744–3751.

Reeves, G., McAdams, K., & Friedel, T., Rand O'Brien. (2003). Acceleration and loss of relativistic electrons during geomagnetic storms. *Geophysical Research Letters*, *30*(10).

Rodriguez, J. (2014a). GOES 13-15 MAGE/PD pitch angles algorithm theoretical basis document, version 1.0. *Boulder, CO: NOAA National Geophysical Data Center. Retrieved from http://www. ngdc. noaa. gov/stp/satellite/goes/documentation. html*.

Rodriguez, J. (2014b). GOES EPEAD science-quality electron fluxes algorithm theoretical basis document. *NOAA Nat. Geophys. Data Center*.

Roederer, J. G. (1967). On the adiabatic motion of energetic particles in a model magnetosphere. *Journal of Geophysical Research*, *72*(3), 981–992.

Schulz, M., & Lanzerotti, L. (1974). Physics and chemistry in space. *Particle Diffusion in the Radiation Belts*, *7*.

Shprits, Y., Daae, M., & Ni, B. (2012). Statistical analysis of phase space density buildups and dropouts. *Journal of Geophysical Research: Space Physics*, *117*(A1).

Shprits, Y., Drozdov, A., Spasojevic, M., Kellerman, A., Usanova, M., Engebretson, M., ... others (2016). Wave-induced loss of ultra-relativistic electrons in the Van Allen radiation belts. *Nature communications*, *7*, 12883.

Shprits, Y., Elkington, S., Meredith, N., & Subbotin, D. (2008). Review of modeling of losses and sources of relativistic electrons in the outer radiation belt I: Radial transport. *Journal of Atmospheric and Solar-Terrestrial Physics*, *70*(14), 1679–1693.

Shprits, Y., Kellerman, A., Aseev, N., Drozdov, A., & Michaelis, I. (2017). Multi-MeV electron loss in the heart of the radiation belts. *Geophysical Research Letters*, *44*(3), 1204–1209.

Shprits, Y., Kellerman, A., Kondrashov, D., & Subbotin, D. (2013). Application of a new data operator-splitting data assimilation technique to the 3-D VERB diffusion code and CRRES measurements. *Geophysical Research Letters*, *40*(19), 4998–5002.

Shprits, Y., Kondrashov, D., Chen, Y., Thorne, R., Ghil, M., Friedel, R., & Reeves,

G. (2007). Reanalysis of relativistic radiation belt electron fluxes using CRRES satellite data, a radial diffusion model, and a Kalman filter. *Journal of Geophysical Research: Space Physics*, *112*(A12).

Shprits, Y., Subbotin, D., Drozdov, A., Usanova, M., Kellerman, A., Orlova, K., ... Kim, K. (2013). Unusual stable trapping of the ultrarelativistic electrons in the Van Allen radiation belts. *Nature Physics*, *9*(11), 699.

Shprits, Y., Subbotin, D., Meredith, N., & Elkington, S. (2008). Review of modeling of losses and sources of relativistic electrons in the outer radiation belt II: Local acceleration and loss. *Journal of Atmospheric and Solar-Terrestrial Physics*, *70*(14), 1694–1713.

Shprits, Y., Subbotin, D., & Ni, B. (2009). Evolution of electron fluxes in the outer radiation belt computed with the VERB code. *Journal of Geophysical Research: Space Physics*, *114*(A11).

Shprits, Y., Thorne, R., Friedel, R., Reeves, G., Fennell, J., Baker, D., & Kanekal, S. (2006). Outward radial diffusion driven by losses at magnetopause. *Journal of Geophysical Research: Space Physics*, *111*(A11).

Singer, H., Matheson, L., Grubb, R., Newman, A., & Bouwer, D. (1996). Monitoring space weather with the GOES magnetometers. In *GOES-8 and Beyond* (Vol. 2812, pp. 299–309).

Spence, H., Reeves, G., Baker, D., Blake, J., Bolton, M., Bourdarie, S., ... others (2013). Science goals and overview of the Radiation Belt Storm Probes (RBSP) Energetic particle, Composition, and Thermal plasma (ECT) suite on NASA's Van Allen probes mission. *Space Science Reviews*, *179*(1-4), 311–336.

Stratton, J., Harvey, R., & Heyler, G. (2012). Mission overview for the Radiation Belt Storm Probes mission. In *The van allen probes mission* (pp. 29–57). Springer.

Su, Z., Xiao, F., Zheng, H., & Wang, S. (2011). CRRES observation and STEERB simulation of the 9 October 1990 electron radiation belt dropout event. *Geophysical research letters*, *38*(6).

Subbotin, D., & Shprits, Y. (2009). Three-dimensional modeling of the radiation belts using the Versatile Electron Radiation Belt (VERB) code. *Space Weather*, *7*(10).

Thorne, R. (2010). Radiation belt dynamics: The importance of wave-particle inter-

actions. *Geophysical Research Letters*, *37*(22).

Thorne, R., & Kennel, C. (1971). Relativistic electron precipitation during magnetic storm main phase. *Journal of Geophysical research*, *76*(19), 4446–4453.

Thorne, R., O'Brien, T., Shprits, Y., Summers, D., & Horne, R. (2005). Timescale for MeV electron microburst loss during geomagnetic storms. *Journal of Geophysical Research: Space Physics*, *110*(A9).

Tsyganenko, N., & Sitnov, M. (2007). Magnetospheric configurations from a high-resolution data-based magnetic field model. *Journal of Geophysical Research: Space Physics*, *112*(A6).

Turner, D., Angelopoulos, V., Li, W., Bortnik, J., Ni, B., Ma, Q., ... others (2014). Competing source and loss mechanisms due to wave-particle interactions in Earth's outer radiation belt during the 30 September to 3 October 2012 geomagnetic storm. *Journal of Geophysical Research: Space Physics*, *119*(3), 1960–1979.

Turner, D., Angelopoulos, V., Morley, S., Henderson, M., Reeves, G., Li, W., ... others (2014). On the cause and extent of outer radiation belt losses during the 30 September 2012 dropout event. *Journal of Geophysical Research: Space Physics*, *119*(3), 1530–1540.

Turner, D., Kilpua, E., Hietala, H., Claudepierre, S., O'Brien, T., Fennell, J., ... others (2019). The response of Earth's electron radiation belts to geomagnetic storms: Statistics from the Van Allen Probes era including effects from different storm drivers. *Journal of Geophysical Research: Space Physics*, *124*(2), 1013–1034.

Turner, D., Shprits, Y., Hartinger, M., & Angelopoulos, V. (2012). Explaining sudden losses of outer radiation belt electrons during geomagnetic storms. *Nature Physics*, *8*(3), 208.

Usanova, M., Drozdov, A., Orlova, K., Mann, I., Shprits, Y., Robertson, M., ... others (2014). Effect of EMIC waves on relativistic and ultrarelativistic electron populations: Ground-based and Van Allen Probes observations. *Geophysical Research Letters*, *41*(5), 1375–1381.

Usanova, M., Mann, I., Bortnik, J., Shao, L., & Angelopoulos, V. (2012). THEMIS observations of electromagnetic ion cyclotron wave occurrence: Dependence on AE, SYMH, and solar wind dynamic pressure. *Journal of Geophysical*

Research: Space Physics, *117*(A10).

Usanova, M., Mann, I., Rae, I., Kale, Z., Angelopoulos, V., Bonnell, J., ... Singer, H. (2008). Multipoint observations of magnetospheric compression-related EMIC Pc1 waves by THEMIS and CARISMA. *Geophysical Research Letters*, *35*(17).

Walt, M. (2005). *Introduction to geomagnetically trapped radiation*. Cambridge University Press.

Wang, D., Shprits, Y., Zhelavskaya, I., Effenberger, F., Castillo, A., Drozdov, A., ... Cervantes, S. (2019). The effect of plasma boundaries on the dynamic evolution of relativistic radiation belt electrons.

West, H., Buck, R., & Walton, J. (1972). Shadowing of electron azimuthal-drift motions near the noon magnetopause. *Nature Physical Science*, *240*(97), 6–7.

Xiang, Z., Tu, W., Li, X., Ni, B., Morley, S., & Baker, D. (2017). Understanding the mechanisms of radiation belt dropouts observed by Van Allen Probes. *Journal of Geophysical Research: Space Physics*, *122*(10), 9858–9879.

Yu, Y., Koller, J., & Morley, S. (2013). Quantifying the effect of magnetopause shadowing on electron radiation belt dropouts. In *Annales geophysicae* (Vol. 31, pp. 1929–1939).